POLITECNICO DI TORINO
Repository ISTITUZIONALE

Buckling developed in 3D printed PLA cuboidal samples under compression: Analytical, numerical and experimental investigations

Original
Buckling developed in 3D printed PLA cuboidal samples under compression: Analytical, numerical and experimental investigations / Torre, Roberto; Brischetto, Salvatore; Rocco Dipietro, Ivan. - In: ADDITIVE MANUFACTURING. - ISSN 2214-8604. - 38:(2021), pp. 1-14. [10.1016/j.addma.2020.101790]

Availability:
This version is available at: 11583/2861156 since: 2021-01-15T15:19:13Z

Publisher:
Elsevier

Published
DOI:10.1016/j.addma.2020.101790

Terms of use:

This article is made available under terms and conditions as specified in the corresponding bibliographic description in the repository

Publisher copyright
Elsevier postprint/Author's Accepted Manuscript

© 2021. This manuscript version is made available under the CC-BY-NC-ND 4.0 license http://creativecommons.org/licenses/by-nc-nd/4.0/.The final authenticated version is available online at: http://dx.doi.org/10.1016/j.addma.2020.101790

(Article begins on next page)

19 April 2024

Buckling developed in 3D printed PLA cuboidal samples under compression: analytical, numerical and experimental investigations

Roberto Torre* , Salvatore Brischetto† and Ivan Rocco Dipietro‡

Department of Mechanical and Aerospace Engineering, Politecnico di Torino, Torino, Italy

Abstract In this work, the behaviour of short-length PLA 3D printed elements under compression is investigated, with a specific focus on buckling. An extensive experimental campaign is conducted on square polymeric columns produced via Fused Filament Fabrication (FFF), with the longitudinal axis oriented in the out-of-plane direction in 3D printing coordinate system. Compressive and tensile mechanical properties of FFF 3D printed PLA are determined; an asymmetry in out-of-plane tensile-compressive behaviour is discussed. The compression of the specimens is monitored using a single camera Digital Image Correlation system, supported by a preliminary validation of its set-up. The slenderness ratio at which the elements start to buckle is identified. The experimental results are compared with three analytical models for buckling prediction in isotropic materials and with linear and non-linear Finite Elements (FE) models. For a broad range of slenderness ratio, the tangent modulus theory gave a good, if conservative, estimation of the critical loads when used with the compressive mechanical properties. Furthermore, the predictions of the non-linear FE models were found to be consistent with the experimental results.

Keywords: Fused Filament Fabrication; Additive Manufacturing; Compression Test; Buckling; Digital Image Correlation; Analytical, Numerical and Experimental Investigation.

1 Introduction

The key strength of Additive Manufacturing (AM) is the possibility to create a component directly after its computer-aided-design (CAD) modelling. The process starts with the slicing of the 3D model into 2D cross-sections in all processes under the definition of AM. These cross-sections are sent to the machine (the 3D printer), which prints them physically and simultaneously combines them into the physical object [1]. Fused Filament Fabrication (FFF) is the most economic and simple AM technology; it has a proven economic efficiency in individual and small productions [2]. In order to shift FFF from prototyping to manufacturing of the final product it is vital that the mechanical properties of the parts are evaluated in order to verify that the component meets the performance criteria [3].

Several authors have investigated the mechanical properties of Fused Filament (FF) fabricated parts. Much attention has been given to low-cost polymers like Acrylonitrile Butadiene Styrene (ABS) and

*Author for Correspondence: Roberto Torre, Department of Mechanical and Aerospace Engineering, Politecnico di Torino, Corso Duca degli Abruzzi 24, 10129 Torino, ITALY. e.mail: roberto.torre@polito.it.

†e.mail: salvatore.brischetto@polito.it

‡e.mail: ivanrocco.dipietro@studenti.polito.it

Polylactic Acid (PLA). Given that standardized procedures and tests for mechanical properties determination of FF fabricated components do not yet exist, many researchers have determined sets of properties following the corresponding test methods for polymers. A novel approach has been proposed by the first two authors: a parallel is suggested between FF fabricated components with a linear infill and long-fiber composites [4]. It is widely accepted that mechanical properties of the components are not the same as the raw filament because they are affected by the printing process and by its custom parameters. Several authors have determined certain mechanical properties under specific circumstances (compound, infill, extrusion temperature, printing speed, etc.). Some other authors have tried to verify the influence of a selected set of printing parameters on a specific set of mechanical properties. In [5], the effect of the infill pattern on the tensile mechanical properties of 3D printed Polyamide (PA) was studied. A criss-cross pattern $[+45°/-45°]$ and a concentric pattern were evaluated on classical dog-bone specimens, which were oriented in different directions in the printing reference system. This study highlighted the differences between data-sheet values and the actual values. Similarly, Zhu et al. [6] proposed a set of tensile and compressive tests, evaluating the effect of printing speed, layer height and filling density on respective strengths. It was found that both the mechanical strengths reach the highest values with thin layers, low printing speeds and 100% infill. The role played by these three factors differed in the two loading configurations. These results were confirmed in [7]. A Design of Experiment was proposed for a parametric study of the mechanical properties in [8] and [9]. Other interesting insights can be found in [10] - [15].

Much less attention has been paid to the determination of the compressive properties of FF fabricated elements. The first two authors studied the compressive properties of FF fabricated PLA in [16] - [18], where the compressive elastic modulus, proportional limit and strength were found. Szczepanik, S. et al. evaluated the compressive properties of ABS and PET, revealing that under a specific set of printing parameters they do not significantly differ from injection molded specimens [19]. In [20] the influence of layer height, infill density and print speed on the compressive strength of FFF PLA specimens was studied. The analysis revealed that the key factor was the infill percentage: high values lead to the highest values of compressive strength. Galatucci et al. proposed in [21] a topologically optimized FFF structural element subjected to compressive load.

In the present work the authors have studied a structural classical problem, *Buckling*, in association with FFF. Several analytical and numerical approaches exist in the literature which allow to predict buckling critical loads; their applicability in this field has not yet been validated as the buckling phenomenon in FF fabricated components has received no attention. The experimental study of buckling has been based on a campaign of compression tests. In order to experimentally quantify the buckling critical loads, the authors considered the experimental methods already available in the literature. Kotsmid et. al. [22] suggested that at least three methods exist. The maximum value of the axial load (LM), the maximum tangent value of the load vs. axial displacement relation (LAD) and the maximum tangent value of the load vs. lateral displacement relation (LLD). Although the three methods provided similar results, it was found that LM was slightly higher than the other two. Furthermore, no significant discrepancies arose between the LAD and the LLD approaches when a linear trend in axial vs. lateral displacement relation was found. Given its simplicity, the LM method has been used by several authors. Shariati et al. [23] drew the axial load vs. axial displacement curve for CK20 cylindrical panels under compression, and determined the buckling load in correspondence to the maximum of the curve. Dundu [24] did the same when analyzing short cold-formed lipped channels. The author found a linear relation between the axial load and the axial displacement up to the maximum load, which was identified as the critical load. Whatever method was used to identify the critical load, almost all the authors monitored the transverse displacement to study the phenomenon. In [25], the buckling of bamboo columns was studied. An experimental campaign was conducted on long specimens, subjected to axial compressive load. Six LVDTs were installed to measure the column deflections, at three different location along the columns' length, in two orthogonal directions. The maximum value of the

compressive load vs. transverse deflection curve was used as critical value. In [26], the compressive load vs. axial displacement and the compressive load vs. transverse displacement curves were compared for buckling investigation in steel columns. As in [27], it was concluded that both curves give lots of information on the phenomenon. The first (with axial displacement) focuses on energy aspects; the second (with lateral displacement) helps in buckling event detection. The "Top of the Knee" approach, analogical to LM method, was used in the report by Nishino et. al [28] in a set of tests on local buckling of plate elements in square columns. As discussed in [29], the "knee" is identified in the curved region of the load vs. transverse deflection curve, separating its lower and upper regions. The buckling load is identified as the load in correspondence with the "top of the knee". Jones however suggests that the localization of the "top" is somehow subjective, as no mathematical definition could be given in order to identify it. Furthermore, the identified load usually does not differ significantly from the maximum load suggested by the LM method. The transverse displacement was also essential for the authors that used the Southwell plot to predict the phenomenon. Turkmen [30] experimentally evaluated the buckling critical loads in steel and aluminium columns. The author monitored and plotted the lateral deflection of several columns vs. the applied load under different loading eccentricities. The actual critical load was deduced as the highest stress value in these plots and compared with the Euler and Southwell predictions. In [31] the Southwell plot method was used to study laminated glass elements in flexural-torsional buckling. The experimental campaign was conducted with a set of different amplitudes of load eccentricities. The Eulerian-predicted critical buckling values and experimentally measured values were found to be in agreement. The same method was used by Borowicz et al. [32] to study web buckling of fibre-reinforced polymers beams in three-point bending tests. A 3D Digital Image Correlation (DIC) system was used to measure the transverse displacements.

Within the framework of this research, Polylactic Acid (PLA) polymer specimens printed using FFF were built, tested under compression and analyzed. A DIC system was used to monitor the compression and get an instantaneous and overall map of axial and transverse displacements and strains. These observations endorsed the use of the LM method. The critical loads were estimated using three analytical models available in the literature for isotropic materials, in order to assess their applicability. Moreover, linear and non-linear finite element models were implemented for further validations of experimental and analytical results. A small set of tensile tests was also arranged in order to understand which mechanical properties were to be used in models for buckling estimation. A comparison between the tensile and the compressive mechanical properties demonstrated an asymmetric behaviour of FF fabricated PLA.

2 Material and testing methods

This section presents the experimental procedure followed for buckling investigation in FF fabricated PLA elements. Both the compressive tests and a small set of tensile tests are described in depth. The technique used for displacements tracking and strain measuring is also discussed.

2.1 Compression Tests

The *Standard Test Method for Compressive Properties of Rigid Plastics*, ASTM D695 [33], provides the guidelines for compression properties investigation in polymers. Its Section 6 reports that the specimens should be in the form of a square prism or a right cylinder, with preferred cross-sections dimensions. For prismatic specimens, the cross-section should be of 12.7 mm by 12.7 mm; for cylinders, the cross-section diameter should be equal to 12.7 mm. Specimens' length depends on the mechanical properties under investigation. It is expressed on terms of slenderness ratio A:

$$A = \frac{L}{\rho} \tag{1}$$

In the framework of the compressive mechanical tests described in ASTM D695, L in Equation 1, is the *overall length* of the specimen. In the framework of buckling phenomenon, the *effective length* L_e of a column is considered, instead, which depends on the overall length L and on the boundary conditions of the specimen under compression. ρ is the *least radius of gyration* of the cross-section. When compressive yield and strength are of interest, the length must be twice the cross section reference size. When the compressive elastic modulus is studied, the slenderness ratio has to be between 11 and 16 [33].

2.1.1 Specimen's geometry

The target of the present paper is the study of the buckling phenomenon; the mechanical properties are not the main focus, even if some of them the will be needed hereinafter. When a column buckles, a sudden lateral deflection manifests at a certain compressive stress. With a specimen in the form of right cylinder, that deflection could manifest in a infinite number of planes due to cross-section symmetry with respect to the longitudinal axis. For sections without such a symmetry, the specimen would deflect in the direction with low moment of inertia [29]. A square prism has therefore a limited number of directions in which the transverse displacement would manifest itself. Section 1 anticipated that the phenomenon will be observed and studied using DIC with a single camera (single observation plane). The square prism has indisputable advantages in this respect: it increases the chances that the deflection would manifest in the observed plane. Once the square geometry has been chosen, its side dimension is set at 12.7 mm. The length of the specimen should be twice the cross section reference size, 25.4 mm, if the compressive strength or yield is under investigation. For compressive modulus determination, the length should be included between 40.4 mm (slenderness ratio equals 11 : 1) and 58.7 mm (16 : 1) [33]. The slenderness ratio is the trigger for buckling, together with the compressive load. Therefore, the

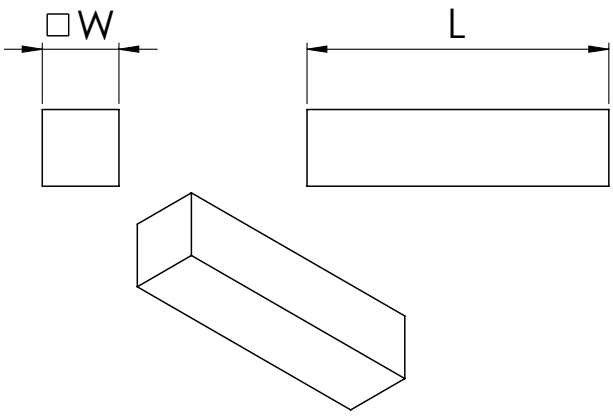

Figure 1: Sketch of a generic compression specimen.

authors investigated the buckling of short columns, letting the length vary between 20 mm to 65 mm with 5 mm increments, thus obtaining 10 different runs. 10 specimens per run were printed. The draw of the generic specimen is shown in Figure 1; the nominal dimensions of the specimens of each run are reported in the second and third column of Table 1. As the buckling of a column is generally described in terms of slenderness ratio, the fourth column of Table 1 reports its nominal value for each run. RUN II is the closest to the geometry for compressive strength and yield determination; furthermore, RUN VII falls midway the slenderness ratio range intended for compressive modulus determination.

RUN	Nominal			Actual					
	W $[mm]$	L $[mm]$	A $[-]$	W_x $[mm]$		W_y $[mm]$		L $[mm]$	
				μ	σ	μ	σ	μ	σ
I	12.7	20	5.45	12.68	0.034	12.71	0.021	19.96	0.023
II	12.7	25	6.81	12.69	0.039	12.70	0.027	24.95	0.043
III	12.7	30	8.17	12.73	0.046	12.75	0.030	29.98	0.022
IV	12.7	35	9.54	12.73	0.037	12.77	0.031	35.06	0.025
V	12.7	40	10.90	12.73	0.045	12.76	0.028	40.10	0.034
VI	12.7	45	12.26	12.72	0.045	12.75	0.031	45.04	0.029
VII	12.7	50	13.62	12.72	0.018	12.74	0.021	50.06	0.030
VIII	12.7	55	14.99	12.76	0.048	12.79	0.040	55.20	0.032
IX	12.7	60	16.35	12.73	0.037	12.74	0.026	60.20	0.028
X	12.7	65	17.71	12.70	0.042	12.74	0.030	65.22	0.022

Table 1: Geometrical dimensions of compressive specimens: μ stands for the mean value of the dimension, σ for its standard deviation.

2.1.2 Specimen's production and printing parameters

For specimens' production, a Creatbot DX 3D printer was used, provided with a rectangular shaped printing volume of $300 \times 250 \times 300$ mm in X, Y and Z directions, respectively. Directions X, Y and Z are those reported in Figure 2, where the printing configuration of a generic run is presented. For each run, a 3D model of the specimen was realized using a CAD Software; the model was then converted into an .stl file. FFF printers usually requires numerical control instructions to be in the format of a .gcode file; an appropriate software was used to build up the instructions. 10 specimens per run were printed all together with the square section lying on the printing floor. As shown in Figure 2, the longitudinal

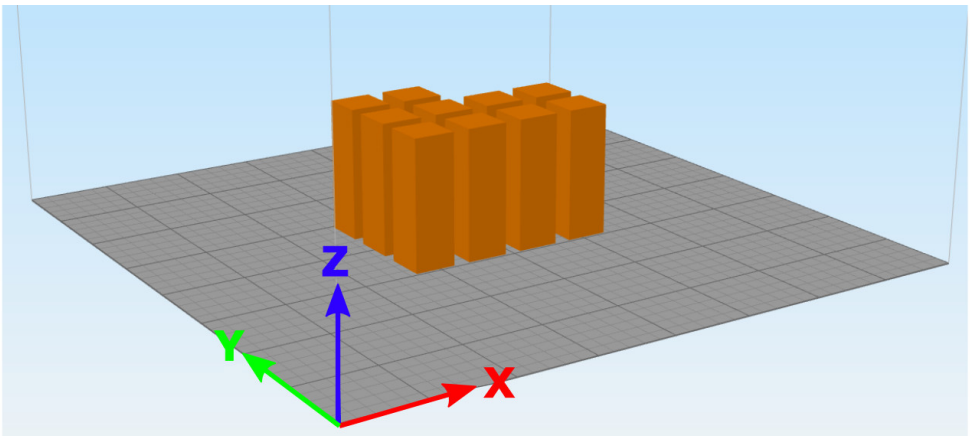

Figure 2: Printing configuration of a generic run of compressive specimens.

axis of each specimen was parallel to Z axis of the 3D printer. Each specimen was positioned so that its side faces were parallel to X and Y axis, respectively. The printing parameters are summarized in Table 2 and here presented. A layer height of 0.1 mm was chosen; the first layer was increased to 0.2 mm to improve the adhesion between the object and the printing plane. An extrusion width of 0.5 mm was set for the deposited filaments. A linear 100% infill was used, with alternated 0° and 90° raster angles. A single peripheral filament was deposited. The extrusion temperature was set to $210°C$; the bed was left at room temperature.

1st layer height	0.20	mm
Gen. layer height	0.10	mm
Nozzle diameter	0.40	mm
Extrusion width	0.50	mm
Infill pattern	linear	-
Infill percentage	100%	-
Perimeters n°	1	-
Raster angle sequence	[0°/90°]	-
Extrusion temperature	210	°C
Bed temperature	room temp.	-

Table 2: Printing parameters used to print compressive and tensile specimens.

2.1.3 Test set-up

A standard compression test requires the compressive stress and strain to be measured at appropriate time intervals. The *compressive stress* is a load per unit area defined by Equation 2:

$$\sigma = \frac{F}{A_0} \tag{2}$$

F is the load sustained by the specimen at a certain moment during the test; A_0 is its minimum original cross section. The *compressive strain* is a dimensionless ratio defined by Equation 3:

$$\epsilon = \frac{\Delta L}{L_0} \tag{3}$$

ΔL is the change in length at a certain moment during the test with respect to the initial length L_0. To use both Equation 2 and 3, the actual dimensions of each specimen were measured. The mean values μ and standard deviations σ are reported, per run, in Table 1.

Before buckling, a uniform distribution of compressive stress and strain is expected along the specimen. In close proximity to buckling that distribution might change, and equation 3 does not allow to assess this. The conventional strain measuring devices have a few critical flaws. A common *strain gauge* would measure only a "localized" stain in the external surface area it is applied to; an *extensometer* would return a single strain, averaged along its gauge length. To get a map of the strains on the external surface of each specimen, a DIC system was used. This choice has a further advantage, as it also allows to get a map of the displacements. A DSLR camera with a 1920×1080 pixels optics was used.

Before being tested, each specimen had to be set up. After removing the last remnants of printing, a random distribution of grays was created on the external surfaces using a black spray. A universal Instron 8800 series testing machine was used. Each specimen was positioned between two plate fixtures, with the longitudinal axis aligned with the load application direction. The tests were executed in displacement control, keeping a testing speed of 1.3 mm/min as per ASTM D695; for simplicity the speed was kept also constant after the yield point. Each specimen was positioned with one out of four lateral surfaces facing the focal plane of the camera. The camera was positioned as close as possible to the specimen in order to dispel focusing issues. The testing machine recorded the applied load and the measured displacement of the movable jaw at 5 Hz. Each test was video-recorded at a frame rate of 30 FPS.

2.2 Tensile Tests

A small set of tensile tests was performed to highlight any differences in the mechanical properties with respect to compression. This was necessary to evaluate which properties had to be used in any

analytical and numerical model for buckling critical stress estimation. The guidelines for tensile properties investigation are given in ASTM D638 [34], the *Standard Test Method for Tensile Properties of Plastics*, where a classical dog-bone specimen is proposed. As the first two authors shown in [4], this geometry proved not to be suitable for out-of-plane properties determination of 3D printed elements. Figure 3 compares the ASTM dog-bone specimen (on the left) and a specimen with constant rectangular

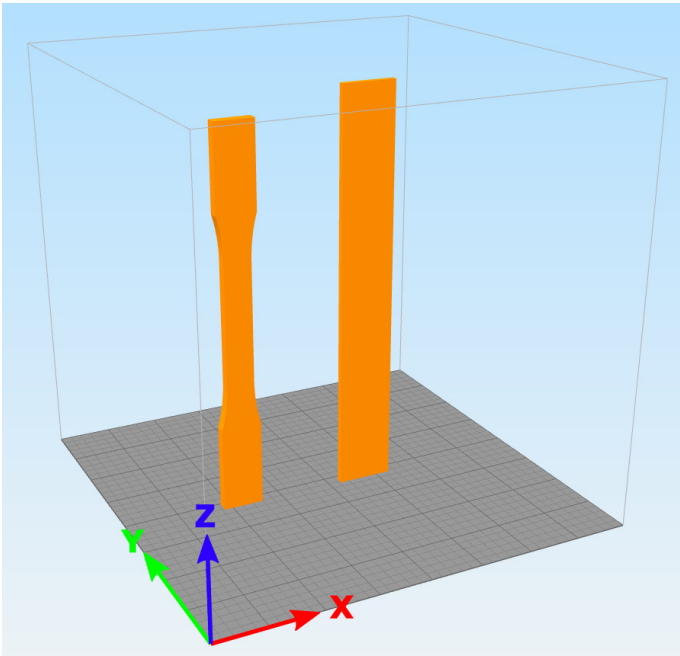

Figure 3: ASTM D638 (left) and ASTM D3039 (right) specimens printing configuration.

cross-section (on the right). The fillet and the cantilevered region in out-of-plane dog bone specimens lead to its premature failure due to stress concentration effects originating in printing defects. The authors followed the *Standard Test Method for Tensile Properties of Polymer Matrix Composite Materials*, ASTM D3039 [35], for tensile out-of-plane properties determination. In the previous work [4], the first two authors proved that the geometry proposed in the latter standard is a valid alternative for tensile properties determination of FF fabricated components with a linear infill.

2.2.1 Specimen's geometry and printing parameters

A rectangular constant cross-section specimen was used. Both the ends were provided with an appropriate set of tabs, consisting of a flat and a tapered section. In [4], the first two authors investigated the geometrical dimensions of the specimen and the tabs. Figure 4 summarizes their nominal values, also reported in the third column of Table 3. Even though the specimen and the tabs are rendered in the same drawing, they were printed separately and than bonded together. To maintain consistency with the compressive tests, the same printing parameters presented in Table 2 were used for tensile specimens, which were printed with their longitudinal axis oriented along Z printing direction. The same printing parameters were also used to separately print supporting tabs. A total number of 5 specimens was produced.

2.2.2 Test set-up

Before each test, a set of four tabs was bonded to each specimen; a bi-component epoxy adhesive was used. The actual dimensions of the cross sections were measured. The mean values μ and the standard

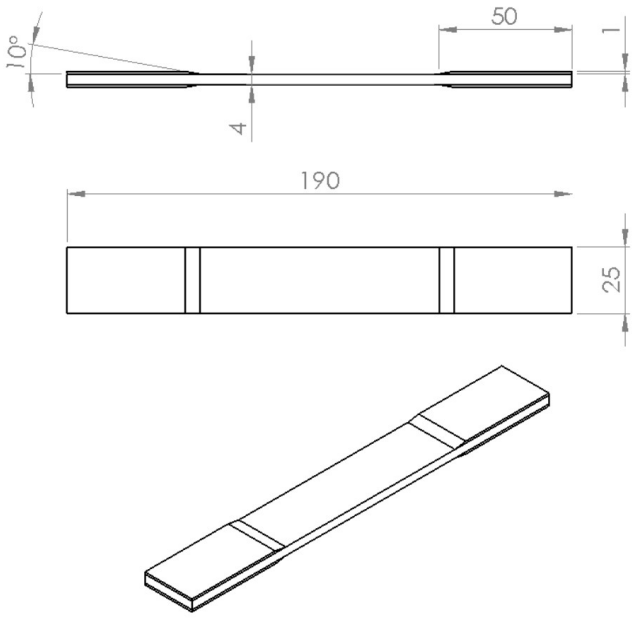

Figure 4: Sketch of a tensile specimen.

				μ	σ
SPCMs.	Overall length	L_0^T	190 mm	-	-
	Width	W^T	25 mm	24.70 mm	0.038 mm
	Thickness	T^T	4 mm	3.57 mm	0.010 mm
TABs.	Overall length	l_0^t	50 mm	-	-
	Width	w^t	25 mm	-	-
	Thickness	t^t	1 mm	-	-
	Taper angle	α^t	10°	-	-

Table 3: Geometrical dimensions of tensile specimens.

deviations σ of the measurements are reported in last columns of Table 3. The tensile specimens were tested with a universal MTS Qtest10 testing machine. Each specimen was positioned into the grips, checking that its longitudinal axis was aligned with the load application direction. The specimens were loaded in displacement control; a speed of 5 mm/min was imposed. The control system of the testing machine recorded at 5 Hz the applied load F and the imposed displacement ΔL. Equation 2 was used to determine the *tensile stress*, with A_0 being the initial narrowest cross-section dimension of the specimen. DIC was used to get a map of the longitudinal strains throughout the specimens. As per the compressive tests, each tensile one was video-recorded with a DSLR camera at a frame rate of 30 FPS.

2.3 Digital Image Correlation set-up

The rationale behind the use of DIC was explained in Subsection 2.1. The basic version of GOM Correlate software was used. Each video is imported into the software, which extracts the frames. The first frame before the test is set as reference image, against which the displacements are measured and the strains calculated. The correlation software produces a displacements and a strains map per analyzed frame. The extraction frequency was lowered to the data acquisition frequency of the testing machine (5 Hz). In this way the load and the displacement-strain information could be linked, as they

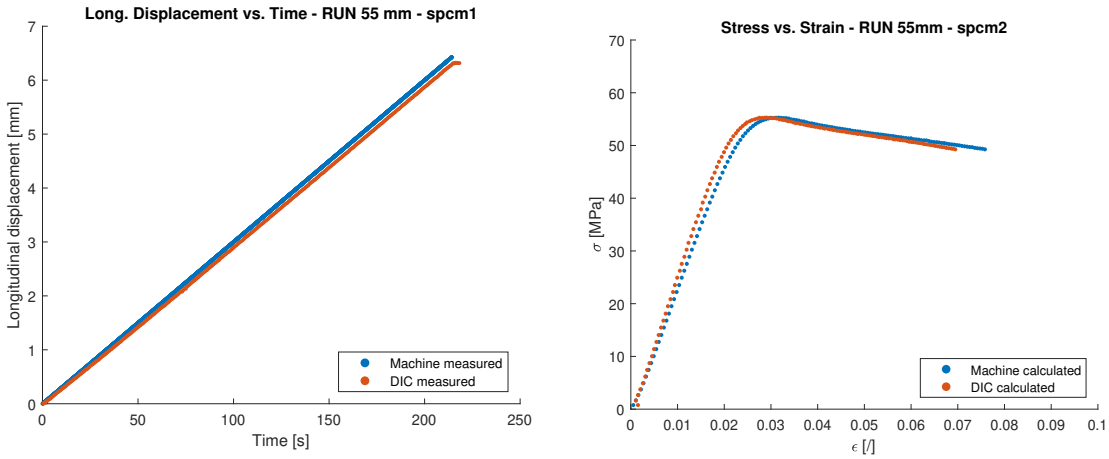

(a) Maximum vertical displacement.

(b) Longitudinal strain.

Figure 5: DIC validation: maximum vertical displacement vs. time (left) and longitudinal strain vs. compressive stress (right) measured in a control specimen.

were sampled at same time intervals. Furthermore, that lowered the computational cost and reduced the noise-oscillation in displacements' measuring. For compressive tests, the area visually occupied by the whole specimen was set as the Region Of Interest (ROI). For tensile ones, the ROI was identified as the area visually occupied by the reduced section of the specimen. The analysis parameters were kept as those suggested by the software: a *facet size* of 19 pixels was set; facets were separated by 16 pixels. To calculate the strain at a certain point, a strain neighborhood is needed; 6 adjacent points were took into consideration. At first step, displacements and strains are calculated in terms of pixel; the scale was set specifying the transverse dimension of each specimen over the reference image. A Matlab tool was implemented to link displacements and strains with the stresses measured by the testing machine, as they are not synced over the time. The testing machine samples the applied load and the imposed displacement as the test starts; the DIC correlates the displacements as soon as the user operates the DSLR camera. The two measures may be synced offsetting the initial frames, in which the displacement maps result in an average null displacement.

2.3.1 DIC Validation

In order to assess the reliability of the DIC setup, a preliminary control was implemented before each run was tested. During compression the longitudinal displacement of a point in the specimen takes different values depending on its relative position with respect to both the fixed (upper) jaw and the movable (lower) one. The maximum longitudinal displacement is located in correspondence to specimen's end section facing the movable jaw. The minimum (zero) displacement is located in correspondence to the opposite end section, facing the fixed jaw. The displacement of the movable jaw is that measured by the testing machine control system. One would expect this displacement to equal that measured via DIC at the corresponding specimen's end section. Figure 5(a) compares the displacement vs. time measured via DIC and that reported by the machine for a control specimen. Both the curves are linear over the time as a constant displacement speed was imposed. A maximum deviation of 3% was found between the two sampling. A further preliminary control was made with respect to DIC calculated strains. Assuming the axial strain is uniformly distributed along specimen's length, it can be calculated by means of Equation 3, using the displacement of the movable jaw given by the machine control system. In Figure 5(b) this strain is compared with the mean axial deformation calculated via DIC, for a control specimen; the stresses are reported by the machine control system. The red curve

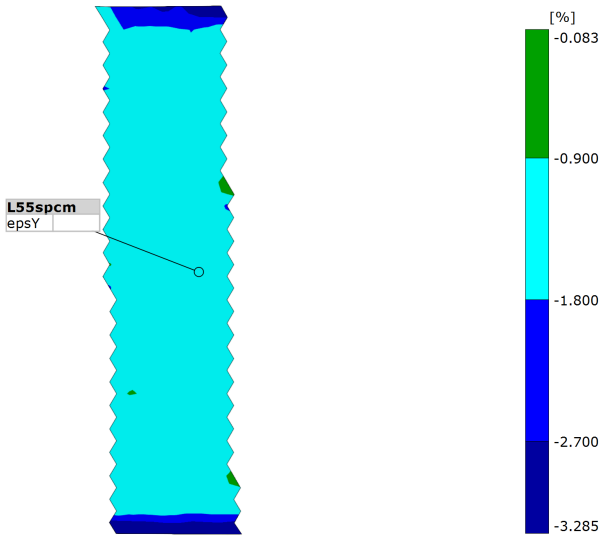

Figure 6: Longitudinal strain map of a 55mm-long control specimen at a given stress level, obtained via DIC.

is obtained with DIC-calculated strains; the blue one considers machine-calculated strains. The trend is the same, even though a slight difference can be noted. At a given instant during the test (at which a given stress corresponds) the DIC seems to underestimate both the maximum vertical displacement and the longitudinal strain. Due to perspective, scene and shadows during the test, the ROI does not overlap completely the front surface of the specimen but lacks a (very) small region at the top and at the bottom. An exact correspondence between machine and DIC measured displacement would have occurred if the ROI covered the specimen up to the top section. The differences in the strains arise from the strain distribution, which is not uniform at specimen's ends, where a higher level of strain concentration manifests, as shown in Figure 6. The validation of the DIC set-up was carried out by means of compressive specimens as tensile ones had no basis for comparison. In tensile specimens the displacement of the movable jaw is different from any of those measured over the reduced section, as the grips end over the tabs.

3 Analytical and Numerical models

The specimens can be generically considered as *columns*. Several analytical models exist that allow the buckling of a column to be studied; at the same time the phenomenon can be evaluated numerically by recourse to FE models. Whether they are analytical or numerical, all of them allow to draw a graph of the critical stress vs. the slenderness ratio. The analytical models that will be considered share some assumptions.

- In terms of materials, the column is made of an *isotropic and homogeneous material*, which is generally true for polymers like PLA. Section 1, however, discussed about the influence of the infill pattern on the mechanical properties of the components, showing that a certain anisotropy may be present.
- In terms of boundary conditions, the *compressive load is supposed to be directed in the axial direction on the column*, with the column being initially *perfectly straight*. In additions *fictionless constrains* and *rigid compressive supports* are considered.
- In terms of geometry, column's cross-section is supposed to be *uniform and constant*.

- The *absence of initial stresses* and the *negligibility of column's weight* are also considered.

Given the limits of real testing scenarios, this section will evaluate the suitability of some analytical models with respect to FF fabricated specimens. Furthermore, a comparison with FE numerical models will be presented.

3.1 Analytical models

Three analytical models are considered; the first two share the same equation [29]:

$$\sigma_{cr}^{E} = \frac{\pi^2 E}{A^2} \tag{4}$$

E is the stiffness coefficient of the material, A the slenderness ratio. As anticipated, in buckling phenomenon A is a function of the *effective length* L_e of the column, calculated multiplying the *overall length* by k, which takes into consideration the boundary conditions. Pinned ends were considered, corresponding to $k = 1$. The effective and the overall lengths coincide. With Equation 4 the *Eulerian critical stress* can be calculated (1st model) using the *Linear Elastic* modulus E_L. In addition to the previous, two more assumptions are made when Eulerian critical stress is calculated:

- The column length is significantly higher than its cross-sectional dimensions.
- The compressive stress does not exceed the proportional limit of the material.

The first assumption is a consequence of the second. Eq. 4 shows that the critical stress increases as the slenderness ratio of the column decreases. Once the critical stress is higher than the proportional limit σ_p, Euler's critical load is no more accurate as the Linear Elastic Modulus is no more representative of material's behavior. Reversing Equation 4, one could determine Euler's critical load to be valid when $A > A_{lim}$, where $A_{lim} = \pi\sqrt{E_L/\sigma_p}$. In other words, this model is capable of describing the *Elastic Buckling*. Within this work, the critical loads so determined will be referred to as $\sigma_{cr}^{L.E}$, where $L.E$ means Linear Euler. It was assumed that, above the elastic limit, Equation 4 could be still used, with the tangent modulus of elasticity E_T in place of E_L (2nd model). This way, the *Tangent Modulus Theory* is obtained [29], which is proved to better approximate the critical load in case of *Inelastic Buckling*. The further assumptions of the 1st model are no more needed. This model assumes that the tangent modulus is applicable to the whole cross-section of the column. Within this work, the critical loads so determined will be referred to as $\sigma_{cr}^{T.M}$, where $T.M$ means Tangent Modulus theory. Last considered model (3rd) is Johnson's empiric formula for low slenderness ratio columns:

$$\sigma_{cr}^{J} = \sigma_y - \frac{\sigma_y^2 A^2}{4\pi^2 E_L} \tag{5}$$

σ_y is the yield stress of the material. Johnson's equation is considered to create a new failure region, starting from a transition point in Linear Euler's formula. The transition point can be found equalling the two critical stresses, $\sigma_{cr}^{J} = \sigma_{cr}^{L.E}$, thus obtaining the transition slenderness ratio $A_{trans} = \pi\sqrt{2E/\sigma_y}$.

3.2 Numerical models

Buckling in simple and complex structures can be investigated with several numerical models. FE models under Nastran&Patran were considered and their suitability for FF fabricated components was evaluated. Post-buckling behaviour was not studied; two kind of FE solutions were considered: linear static (SOL 101) and non-linear static (SOL 106). SOL 101 considers a linear elastic constitutive model for material properties definition, despite of the actual stress field. It is unable to consider the changing slope of the stress vs. strain curve. An eigenvalue problem is solved: the eigenvector

represents the buckled shape of the structure; the eigenvalue a multiplying factor for the applied load leading to its critical value. Similarly to Linear Euler model, SOL 101 is a simple and effective way to study Elastic Buckling, which is typical of high slenderness ratio elements. SOL 106 takes into account an elastoplastic constitutive model, which is defined in terms of the actual stress-strain curve of the material. Analogously to Tangent Modulus theory and Johnson's formula, SOL 106 is more adequate to study Unelastic Buckling, typical of low slenderness ratio elements. The analysis is carried out by means of two subsequent steps. In the first one the applied load is gradually increased until convergence problems occur. The highest value represents either the maximum sustainable load or a rough evaluation of the critical load. In the second step an eigenvalue problem is solved using as applied load the previous value. As before, the eigenvector gives the buckled shape of the structure; the eigenvalue a multiplying factor for the applied load.

The problem is essentially unidirectional, as columns compressed along their longitudinal axis are considered. To draw the critical loads vs. slenderness ratio curve, a set of equidistant column lengths in the range $20 - 120$ mm was considered. Each column was geometrically defined as a segment, representing its longitudinal axis. 1D BEAM elements were used; in their definition, the inertial properties were considered defining a square cross section with side dimension of 12.7 mm. To maintain consistency, the structure reference system was modified to be the same as that discussed in Figure 2. BAR2 topology was used to mesh each column; 40 elements with two nodes were defined in each model after the convergence of the solution was preliminary evaluated. The boundary conditions were defined as follows. The displacements in X, Y and Z directions were constrained in the top end node; in the bottom end node the X and Y displacement components were constrained, while a compressive force was defined acting along Z. To excite the first buckling mode, an unit transverse force was applied in X direction in the middle node. PLA was considered as an isotropic material, using the out-of-plane compressive mechanical properties experimentally determined.

4 Results

This section discusses how the mechanical data were derived, from both the compressive and the tensile tests, and post-processed. The way the buckling was observed is also presented. Figures 7(a)-10(a) show the compressive stress vs. longitudinal strain diagrams for a specimen per family. 100 compressive specimens were tested, 10 per run. Due to space constraint a single representative graph is considered. In these graphs the stress is calculated according to Equation 2; the strain is the mean axial deformation calculated via DIC. All the specimens showed the classical linear elastic behaviour. A (local) maximum is quickly reached after the curve deviates from linearity. There, an increase of strains occurs without an increase in stress. In ASTM D695, the stress measured at that point is defined as the yield stress of the specimen. After yielding, each specimen behaves differently as a function of its length. In shortest specimens (RUN I-III, Figures 7(a)-7(c)) the stress settles down for a wide range of strains after the local maximum, then starts growing again. In RUN IV specimens, Figure 8(a), that ascent is not present, and the stress keeps almost constant for a wide range of deformations. Longer specimens (RUN V-X, Figures 8(b) - 10(a)) manifested a still different behaviour; after the local maximum the stress slightly decreases as the strain increases. This behaviour seemed to be linked to specimens' failure modes. As it will be shown hereinafter, the $20 - 30$ mm-long specimens simply compressed manifesting barreling. A double barreling compression was found for 35 mm-long specimens. As the length of the specimen increased, buckling appeared. In $40 - 65$ mm-long specimens, barrelling completely disappeared, in favour of a marked buckling. Some graphs exhibit a few bandwidth (eg. Figure 7(a)); those singularities are mainly due to subsequent readjustments of the specimen within its seat. All the specimens showed a more or less pronounced initial behaviour, excluded from the actual analysis as it is a representation of initial realignments.

Figure 11 show the tensile stress vs. longitudinal strain curve for a selected specimen. The stress is

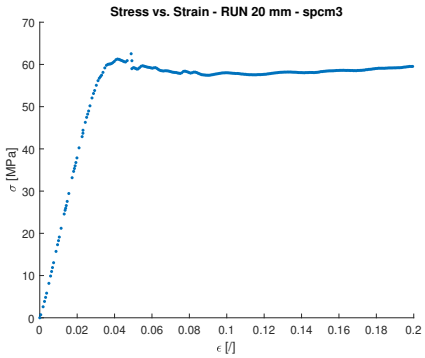

(a) I ($20mm$).

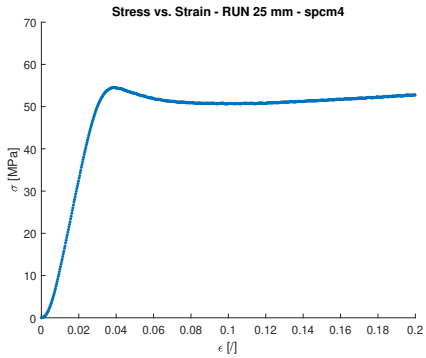

(b) II ($25mm$).

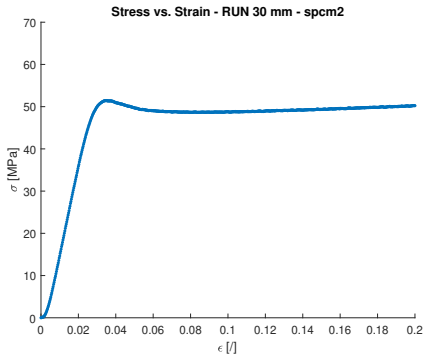

(c) III ($30mm$).

Figure 7: Experimental compressive stress vs. longitudinal strain curve: RUN I, II, and III.

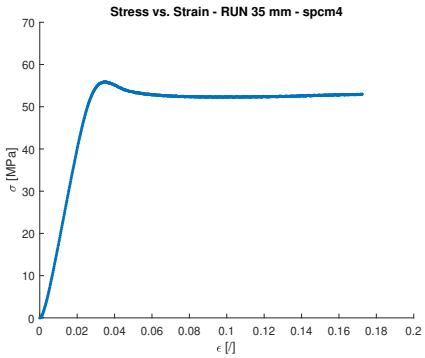

(a) IV ($35mm$).

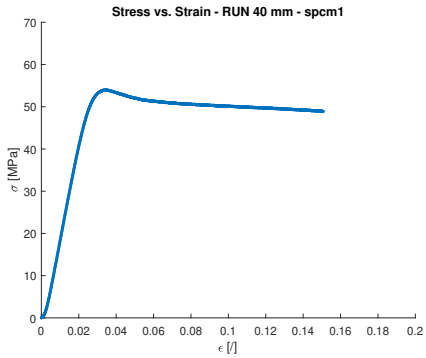

(b) V ($40mm$).

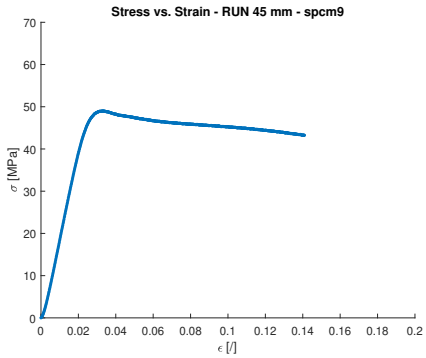

(c) VI ($45mm$).

Figure 8: Experimental compressive stress vs. longitudinal strain curve: RUN IV, V, and VI.

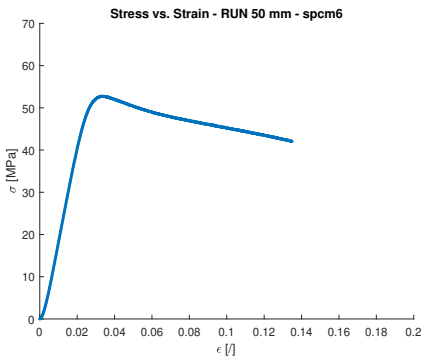

(a) VII ($50mm$).

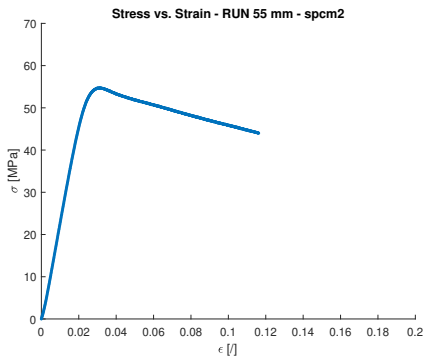

(b) VIII ($55mm$).

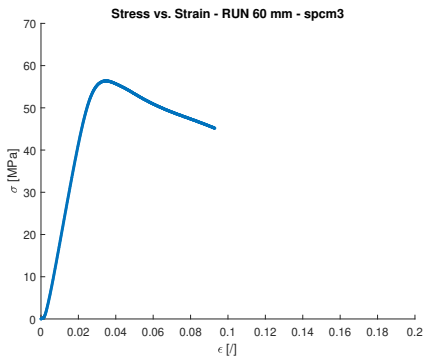

(c) IX ($60mm$).

Figure 9: Experimental compressive stress vs. longitudinal strain curve: RUN VII, VIII, and IX.

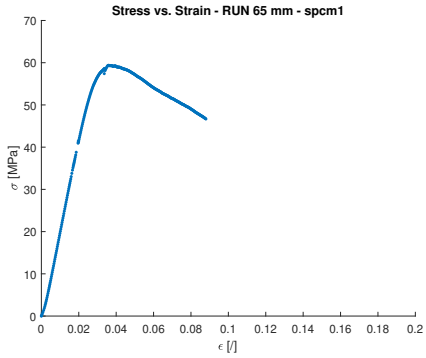

(a) X ($65mm$).

Figure 10: Experimental compressive stress vs. longitudinal strain curve: RUN X.

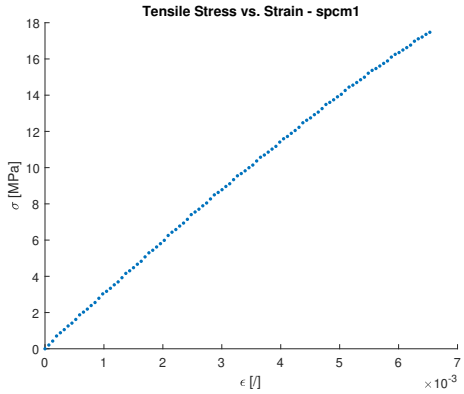

Figure 11: Experimental tensile stress vs. longitudinal strain for a tensile specimen.

calculated according to Equation 2, using the initial cross section dimensions of the specimen; the strain is obtained averaging the longitudinal strains calculated via DIC. It can appreciated how different the tensile response of 3D printed PLA is from the compressive one. All the specimens broke abruptly after a slight deviation from the classical linear elastic behavior. All the specimens proved to be extremely brittle.

4.1 Mechanical properties determination

This subsection explains how the compressive and the tensile mechanical properties were determined. In this paragraph, when talking about compression reference is made to the mechanical properties of each run, and not to the compressive mechanical properties of the material. As each run has fixed cross-section dimensions, but arbitrary length, the calculated properties may not be consistent with the requirements of ASTM standard [33]. Figures 7(a)-10(a) were determined for each specimen (10 specimens per run, 100 total tests). Each curve lead to a set of mechanical properties, per specimen. The *compressive elastic modulus* E_l^C was calculated by a linear interpolation with the least squares method within an iterative procedure. The first iteration considered an initial range of stress-strain values; in subsequent iterations the range of the considered values was gradually increased. Each iteration allowed to calculate new coefficients, then averaged with the previous. The procedure ended when the difference between the new coefficient and the last averaged value was greater than 3%. The stress at which the procedure stopped was identified as the *compressive proportional limit*, σ_p^C. At (local) maximum stress that appears in each curve, an increase of strains occurs without an increase in stress. The stress measured at that point was defined as the *compressive yield stress* σ_y^C, according to

RUN	Length [mm]	E_l^C [MPa]	σ_p^C [MPa]	σ_y^C [MPa]
I	20	1951	49.98	59.89
II	25	1997	45.97	52.95
III	30	2151	43.62	52.18
IV	35	2262	46.64	55.17
V	40	2283	43.90	52.69
VI	45	2226	43.19	50.83
VII	50	2301	45.06	53.08
VIII	55	2312	46.56	53.01
IX	60	2313	46.39	53.58
X	65	2210	45.89	58.04

Table 4: Mean compressive mechanical parameters per run.

COMP.	E_l^C	2301	MPa	Run VII
	σ_p^C	45.97	MPa	Run II
	σ_y^C	52.95	MPa	Run II
TENS.	E_l^T	2894	MPa	-
	σ_p^T	13.06	MPa	-
	σ_y^T	17.47	MPa	-
	σ_s^T	17.47	MPa	-

Table 5: Mechanical properties of PLA.

ASTM D695. The *compressive strength* was not evaluated, as shorter specimens, with rising stress after yield point, were not brought to rupture. The mechanical properties representative of each run were derived averaging among the specimens of that run. Table 4 summarizes the mechanical properties so far determined, per run. Following ASTM D695, the compressive yield is to be determined using 25.4 mm-long specimens. The value found for the second run (25 mm-long) can be considered representative for the printed polymer. The elastic modulus rises with specimen's length, exception made for some local oscillations. Specimens included in the range $40 - 60$ mm in length, however, showed similar values for the elastic modulus. This confirms the slenderness-ratio range required by the standard for the compressive elastic modulus determination. The value found for the seventh run (50 mm-long) can be considered representative of PLA.

The same procedure was adopted for tensile properties determination; the *tensile modulus of elasticity* E_l^T was determined using the same iterative procedure. The stress level at which the procedure ended was reported as the *tensile proportional limit*, σ_p^T; all the specimens abruptly failed slightly above it. No difference could be highlighted between *tensile strength*, σ_s^T, and *tensile yield stress*, σ_y^T. The mechanical properties representative of PLA are summarized in Table 5, distinguishing between compressive and tensile ones.

The tensile modulus of elasticity is 25% higher than the compressive one. Out-of-plane 3D printed PLA proved to be stiffer when loaded in tension, than in compression. Reversely, it sustained much higher loads under compression, than under tension.

4.1.1 Tangent Modulus Determination

PLA compressive *Linear Elastic Modulus* and *Yield Stress* are reported in Table 5. Linear Euler model and FE SOL 101 require the Linear Elastic Modulus; Johnson's formula requires the yield stress, also. To evaluate the critical stress with the Tangent Modulus theory, the *Tangent Modulus* is required, which

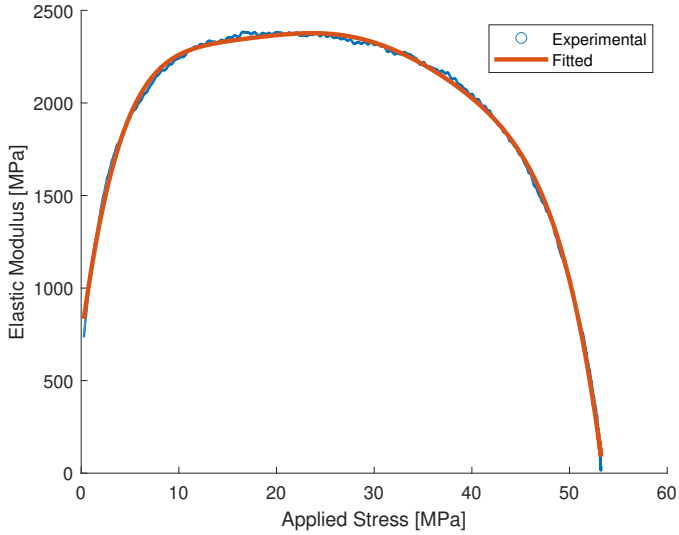

Figure 12: Experimental tangent modulus of 55mm-long specimens.

represents the slope of the stress-strain curve at any stress level. RUN VII specimens were considered, as they were used to determine the Linear Elastic Modulus. A Matlab script was implemented to build a representative curve for the run. Each test was conducted in displacement-control, and strains were calculated directly from the displacements. For the specimens of a single run, the displacements and the strains are in sync over time. The calculated stresses were averaged among RUN VII specimens, leading to a single stress-strain curve. A certain number of equidistant points up to the maximum stress was considered; the tangent modulus was calculated with the central difference method. A 6-th degree polynomial was used to interpolate the Tangent Modulus vs. Applied Stress relation. The dotted blue line of Figure 12 shows the experimental values of the Tangent Elastic Modulus; the red line represents the polynomial fit. The Modulus quickly increases up to an applied stress of 10 MPa. Than, it keeps almost constant for a wide range of stresses. A sudden drop manifests from an applied stress of about 45 MPa, leading to almost nil Modulus near the maximum Applied Stress, at about 53 MPa. This behaviour is coherent with the values presented in Table 4 for RUN VII σ_p^C and σ_y^C.

4.2 Buckling observation

Buckling was observed in terms of transverse displacements. Figures 13-15 show the maps of the transverse displacement at different stages of the test for a 20 mm-long specimen, a 35 mm-long specimen and a 55 mm-long one, respectively. Before the maximum sustained load σ_{MAX} is reached, the stage is identified by the load level, as a percentage. Then the stage is identified in terms of the elapsed time after (AFT) the maximum value was recorded. The displacement-field is superposed to the instantaneous deformed shape of the specimen. The transverse displacement has an initial symmetric pattern with respect to the longitudinal axis in all the three specimens. Figure 13 shows that the transverse displacement keeps symmetric in 20 mm-long specimens at the maximum stress and in the subsequent stages. A *barelling* compression mode manifested itself. The same behaviour was found for 25 mm and 30 mm long specimens. 35 mm long specimens compressed with a *double barelling* mode; this can be partially detected in Figure 14. The lower bulge could be recorded on the front-facing surface of the specimen; the upper one manifested on the back side. Nevertheless, the transverse displacements kept symmetric with respect to the longitudinal axis, at the maximum stress and in the remainder of the test. Figure 15 shows the behaviour of longer specimens. As soon as the actual load

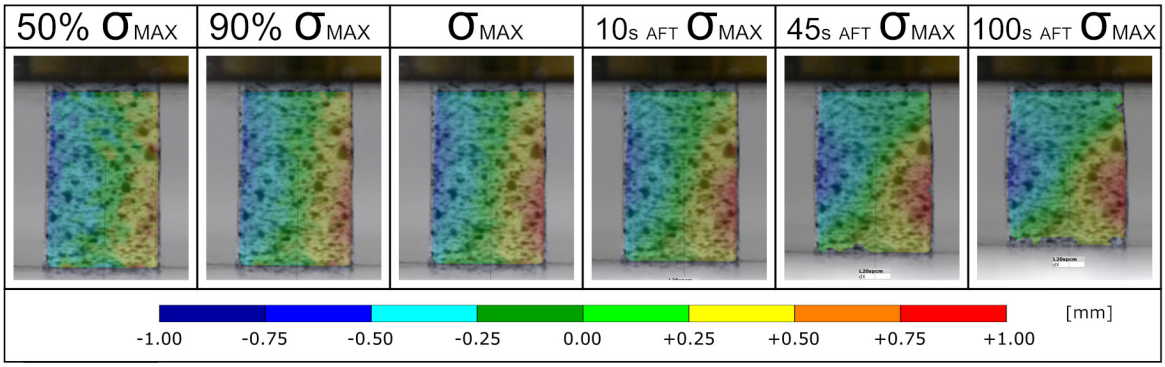

Figure 13: Transverse displacement map for a 20mm-long specimen at different moments during compression, obtained via DIC.

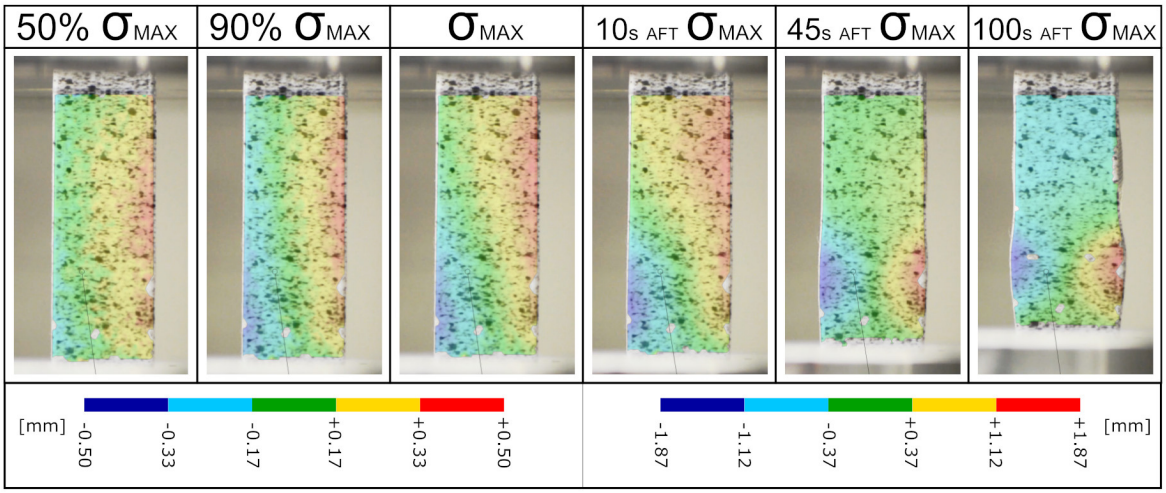

Figure 14: Transverse displacement map for a 35mm-long specimen at different moments during compression, obtained via DIC.

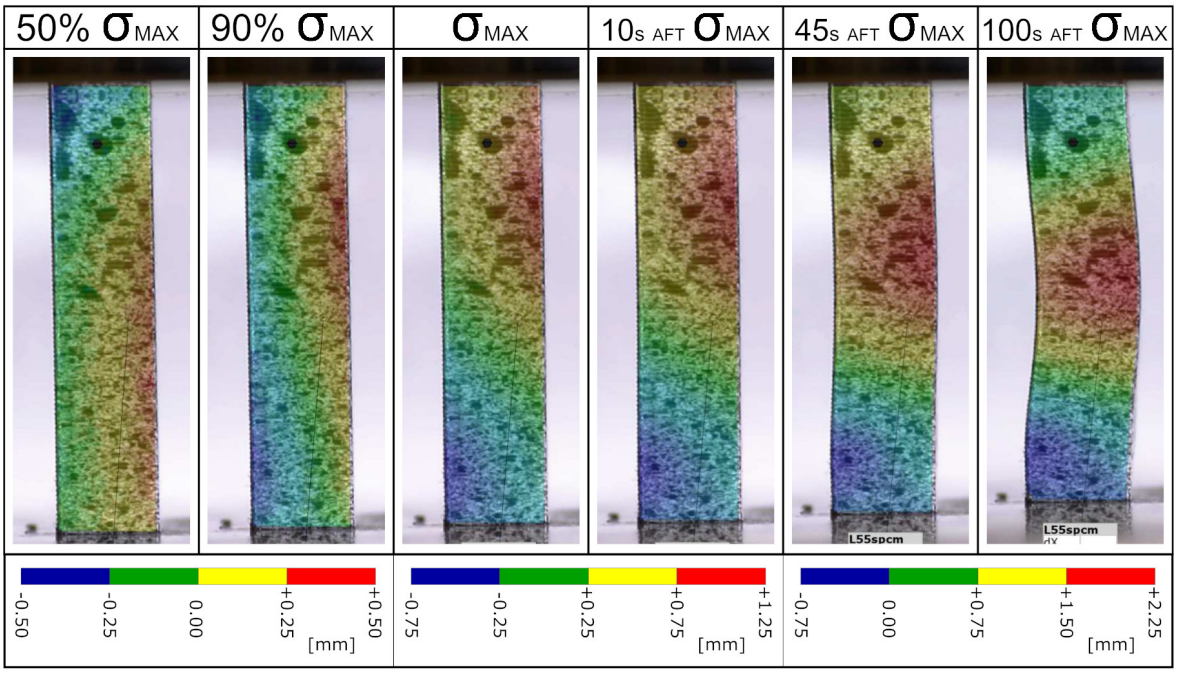

Figure 15: Transverse displacement map for a $55mm$-long specimen at different moments during compression, obtained via DIC.

approached its maximum value, the transverse displacements diverged from symmetry. The highest values concentrated approximately in the middle section of the specimens, resulting in the classical *buckling* mode in the latest stages of the tests.

Figures 16(a)-19(a) show the transverse displacement vs. the applied load for a representative specimen per run. The lateral deflections were tracked in the points they assumed their maximum positive and minimum negative values. Two control points were considered per specimen, one facing the right side, one the left. The transverse displacement is initially symmetric: the right control point moves towards the right, the left one toward the left. This behaviour continues after the local maximum stress for shorter specimens ($20 - 35$ mm-long). For longer specimens, 40 mm-long onwards, shortly before the local maximum stress one of the two control points reverse the direction of its transverse displacement. Each graph can be divided in two sections. The first section is linear and very steep; an initial negligible transverse displacement manifests itself. Once a certain high stress level is reached the

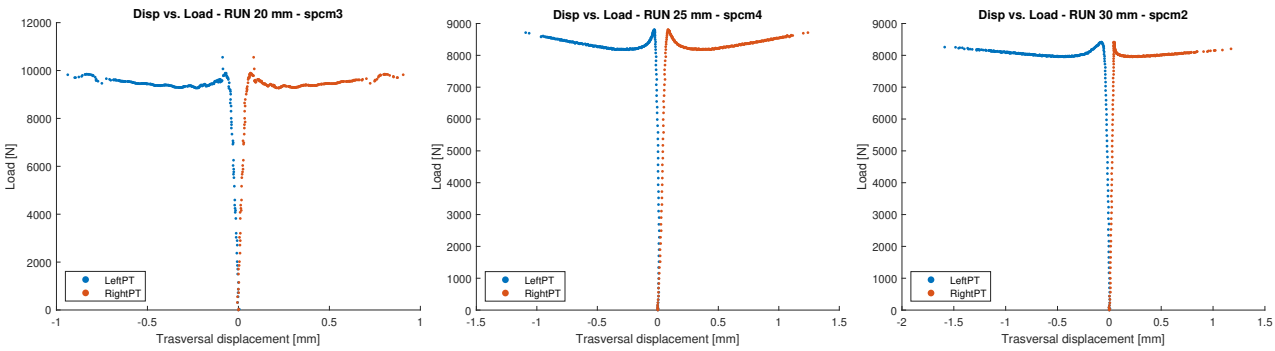

(a) I ($20mm$). (b) II ($25mm$). (c) III ($30mm$).

Figure 16: Experimental transverse displacements vs. compressive load: RUN I, II and III.

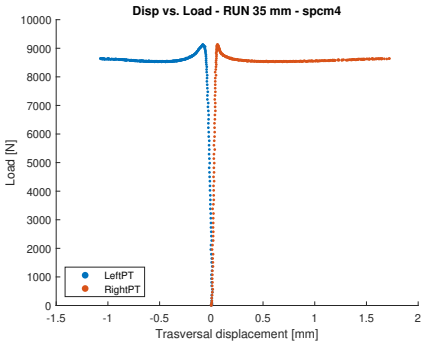

(a) IV ($35mm$).

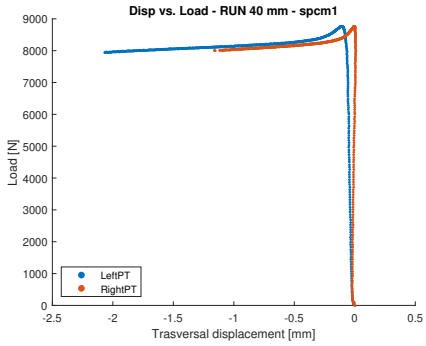

(b) V ($40mm$).

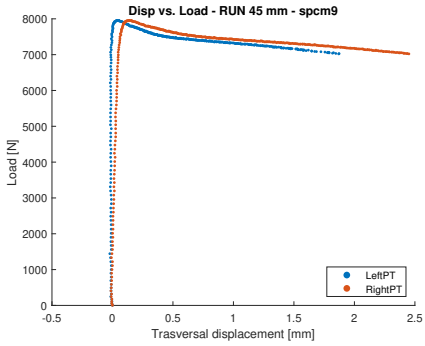

(c) VI ($45mm$).

Figure 17: Experimental transverse displacements vs. compressive load: RUN IV, V and VI.

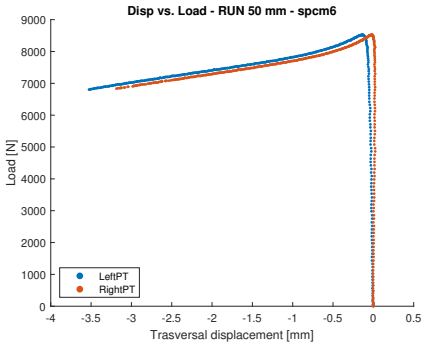

(a) VII ($50mm$).

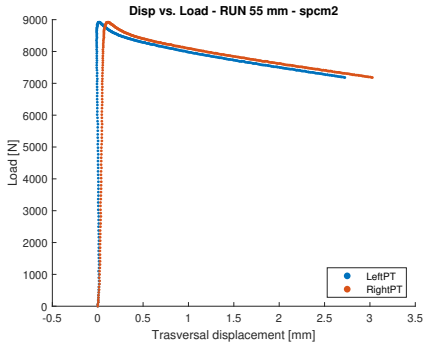

(b) VIII ($55mm$).

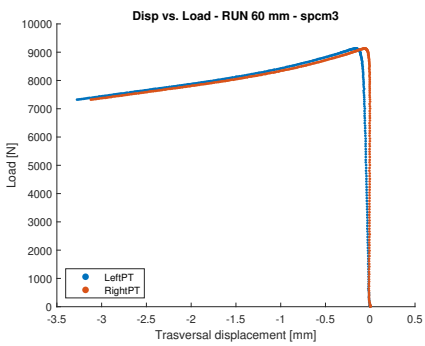

(c) IX ($60mm$).

Figure 18: Experimental transverse displacements vs. compressive load: RUN VII, VIII and IX.

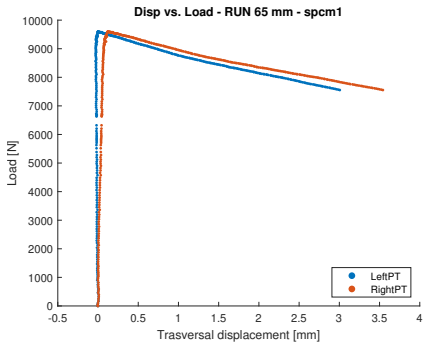

(a) X ($65mm$).

Figure 19: Experimental transverse displacements vs. compressive load: RUN X.

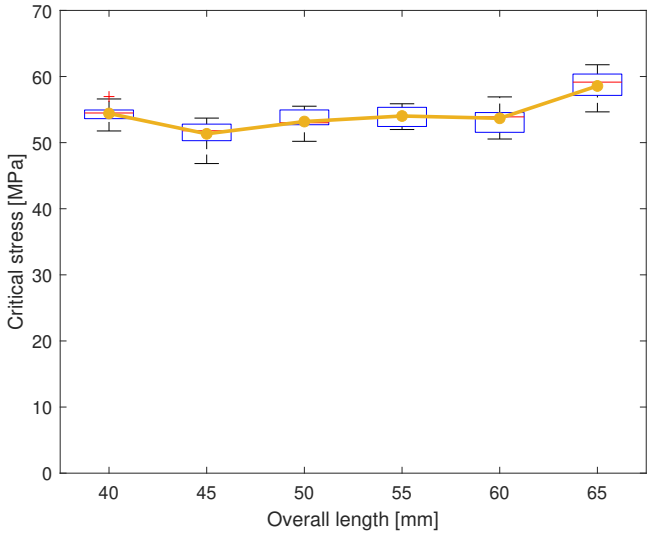

Figure 20: Experimental critical load vs. overall length.

transverse displacement quickly increases as the test continues. This is coherent with the observations on the yield stress, located in correspondence to the (local) maximum stress. In view of a plastic buckling, for those specimens that buckled, the critical load was determined as the stress value corresponding to the junction point of the two sections. The yield stresses reported in Table 4 assume an additional meaning for those specimens that buckled: they also represent the specimens' critical load as their shape suddenly changed at that value.

5 Discussion of results

For the specimens that buckled, the experimental relationship between critical load and specimens' length is shown in Figure 20; a boxplot is presented for each run that buckled. The horizontal red lines represent the median values; the lower and the upper horizontal blue lines represent the Q1/25th Percentile and the Q3/75th Percentile, respectively. Defining as $IQR = Q3 - Q1$ the Interquartile Range of the run, the upper and the lower horizontal black lines represent the $Q3 + 1.5 * IQR$ and the $Q1 - 1.5 * IQR$ values, respectively, enclosing the 99.3% of the values. The orange lines overlayed to boxplots represent the mean values. The critical stresses do not differ significantly among them, exception made for the 45 mm-long and the 65 mm-long specimens. The boxplot of the 45 mm-long specimen shows that this anomaly could be related to the minimum value, which is significantly distant from the mean and the median ones. It is certainly interesting the critical load of 65 mm-long specimens, higher than those found for shorter specimens.

5.1 Critical load vs. Slenderness ratio prediction

The relation between the critical stress and the slenderness ratio can now be predicted by the analytical and numerical models presented in Section 3, as all the mechanical quantities required in the models have been determined. As shown in Table 5, 3D-printed PLA had different responses in tensile and in compressive tests. It was unknown whether the tensile or the compressive mechanical properties had to be used in the analytical models. The tensile strength of out-of-plane 3D printed PLA is significantly lower than the critical stresses presented in Figure 20. This makes the Johnson and the Tangent Modulus theories not applicable, if used with tensile mechanical properties. Given Equation 5, the

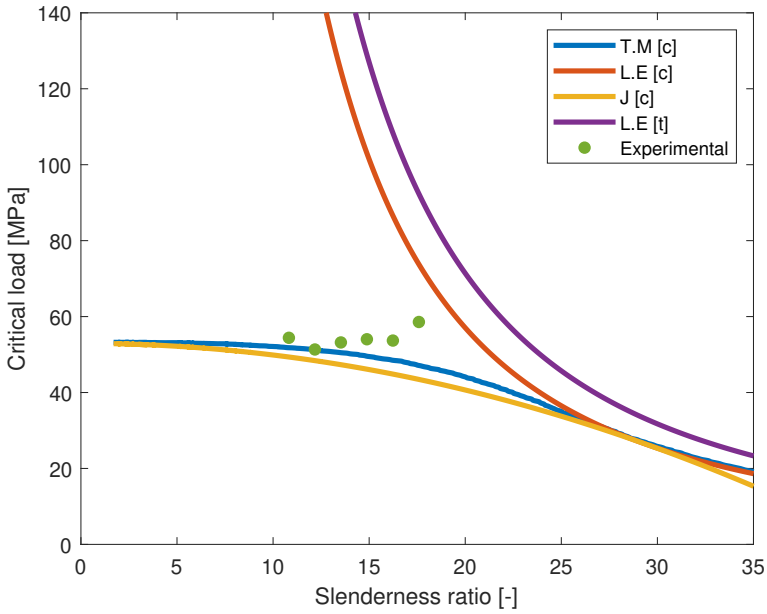

Figure 21: Analytical estimations of critical stresses vs. Experimental values.

first would lead to critical stresses lower than the tensile yield modulus which is, in turn, extremely lower than the experimentally measured critical stresses. At the same time, the second model cannot be computed as the Tensile Tangent Modulus could not be evaluated for stresses higher than the yield point. The compressive mechanical properties instead allow all the three models to be implemented. Using the values reported in Table 5, the limit and the transition slenderness ratios can be determined:

$$A_{lim} = \pi\sqrt{\frac{E_L^C}{\sigma_p^C}} = 22.23 \quad , \quad A_{trans} = \pi\sqrt{\frac{2E^C}{\sigma_y^C}} = 29.29 \tag{6}$$

As shown in Table 1, the slenderness ratio of all the runs is less than A_{lim}, therefore less of A_{trans}. One would expect Linear Euler formula not to be aligned with experimental data and to give very high critical stresses. On the contrary, Tangent Euler an Johnson's models should produce closer results.

The relations driven by the Linear Euler model and by Johnson's formula are trivial; a simple substitution of several slenderness ratio values leads to determine the corresponding critical stresses. Tangent Modulus theory is more critical, as the tangent modulus changes with the stress itself. As the relation between the applied stress and the modulus has already been determined (see Figure 12), Equation 4 was used reversely. For each pair of values (stress-modulus) it was determined the slenderness ratio at which that stress would have been critical. Figure 21 compares the experimental critical loads with the three models' predictions. The Tangent Modulus theory and the Johnson's model are computed using the compressive mechanical properties [c], while the Linear Euler model is computed using the tensile and the compressive mechanical properties, [t] and [c], respectively. Linear Euler model gives the highest critical stresses, as farthest from the experimental values as the slenderness ratio decreases. This is even more pronounced when the tensile linear elastic modulus is used. Johnson's formula and Tangent Euler model are closer to the experimental values. The actual critical stresses follow quite closely Tangent Euler's curve. A certain fluctuation around it is present, and critical stresses always keep a little bit more higher than Tangent Modulus Theory estimation.

For FE SOL 101, the linear elastic constitutive model was defined using the compressive modulus of elasticity reported in Table 5. For the Poisson ratio, PLA typical value of 0.3 was considered. For FE SOL 106, the Elastoplastic constitutive model was completed providing the stress vs. strain curve determined for RUN VII specimens. Figure 22 compares the critical stress vs. slenderness ratio relation

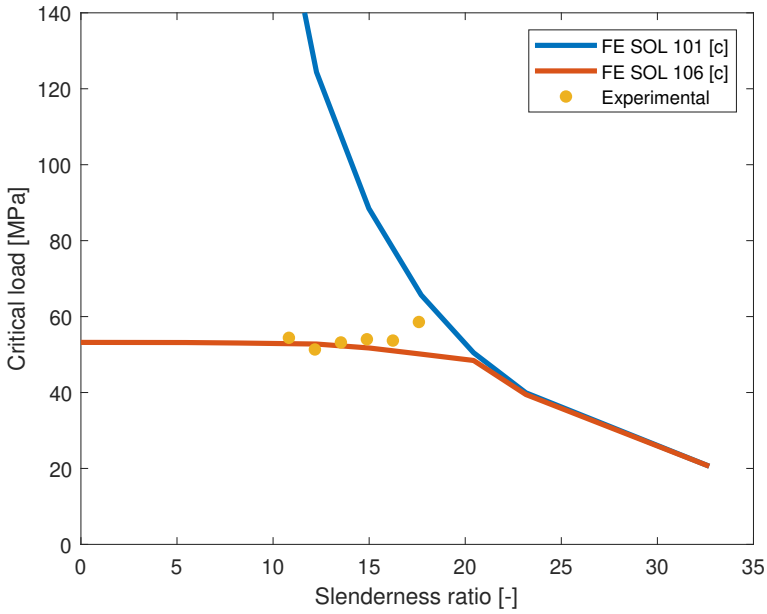

Figure 22: Numerical (FE) estimations of critical stresses vs. Experimental values.

predicted by the FE models and the experimentally determined values. In line with expectations, the linear FE model failed to predict buckling loads at low slenderness ratio. The estimations of the non-linear FE model were found to be consistent with the actual values: a certain fluctuation of the experimental values is present around the SOL 106 curve.

6 Conclusions

This paper analyzed PLA 3D printed elements under compression, with a specific focus on buckling. The authors determined the compressive mechanical properties in the out-of-plane printing direction, and showed they significantly differ from the tensile properties along the same direction. Out-of-plane FF fabricated PLA proved to be 25% stiffer under traction than under compression; tensile specimens failed at lower stress levels than compressive ones. The authors conducted an experimental campaign for a wide range of slenderness ratios in the field of short columns. DIC was used to evaluate the longitudinal stain and the transverse displacements. A preliminary assessment of the set-up was conducted. This tool allowed to evaluate when buckling occurred. Buckling manifests from a slenderness ratio of approximately 9.5. Longer columns buckled, with an almost constant critical load, which did not significantly differ from the yield stress. The compressive mechanical properties needed to be determined in order to use both classical theories of buckling prediction and numerical models. Linear models, both analytical and numerical, are unable to describe the phenomenon, as buckling did not occur in linear material field. When the material non linearity is introduced, both the analytical and the numerical models give consistent estimations, providing a good prediction of the phenomenon in non-linear material field. SOL 106 FE model nearly overlaps with the experimental values, while Tangent Modulus theory keeps a bit more conservative, suggesting lower values. The empirical Johnson's formula has as upper limit value the yield stress, but considers the linear elastic modulus in its formulations. Consequently it keeps close to the experimental values, but consistently below the others models.

The present work can be considered as a starting point for buckling investigation in FF fabricated components. It should verified that, and with what trend, the critical load would decrease with an increase of slenderness ratio. An extension to a wider range of slenderness ratios will be therefore accomplished. As some anisotropy has been demonstrated in FFF, the compressive behaviour so far

determined might not be representative of any configurations. Buckling phenomenon should also be investigated for elements built with the longitudinal axis parallel to the printing plane.

Funding This research did not receive any specific grant from funding agencies in the public, commercial, or not-for-profit sectors.

References

[1] S. Vyavahare, S. Teraiya, D. Panghal, S. Kumar, Fused Filament Fabrication: a review. *Rapid Prototyping Journal*. 26(1) (2020) 176-201. https://doi.org/10.1108/RPJ-04-2019-0106.

[2] C. Gavrus, Economic Efficiency of Using Rapid Prototyping Technology. *Applied Mechanics and Materials*. 371 (2013) 210-214. https://doi.org/10.4028/www.scientific.net/AMM.371.210.

[3] A. Bellini, Mechanical characterization of parts fabricated using Fused Filament Fabrication. *Rapid Prototyping Journal*. 9(4) (2003) 252-264. https://doi.org/10.1108/13552540310489631

[4] R. Torre, S. Brischetto, C.G. Ferro, P. Maggiore, Characterization, in Analogy with Composites Embedding Unidirectional Long Fibres, of PLA Specimens Produced via FFF Printing Process. *Proceedings of the 21st International Conference on Composite Structures (ICCS21)*. International Conference on Composite Structures, Bologna, Italy. (2018). https://doi.org/10.15651/978-88-938-5079-7

[5] I. Ferreira, J. Alves, M. Machado, Effect of layer filling path on mechanical properties of PA and PA-reinforced FFF parts. PMI Conference. (2018). https://doi.org/10.13140/RG.2.2.21586.61124

[6] Z. Yu, Y. Gao, J. Jiang, H. Gu, S. Lv, H. Ni, X. Wang, C. Jia, Study on Effects of FFF 3D Printing Parameters on Mechanical Properties of Polylactic Acid. IOP Conference Series: Materials Science and Engineering. (2018). https://doi.org/10.1088/1757-899X/688/3/033026

[7] M. Sharma, V. Sharma, P. Kala, Optimization of process variables to improve the mechanical properties of FFF structures. *Journal of Physics: Conference Series*, 2nd International Conference on New Frontiers in Engineering, Science & Technology (NFEST), Kurukshetra, Haryana, India. (2019). https://doi.org/10.1088/1742-6596/1240/1/012061.

[8] X. Liu, M. Zhang, S. Li, J. Peng, Y. Hu, Mechanical property parametric appraisal of Fused Filament Fabrication parts based on the gray Taguchi method. *International Journal of Additive Manufacturing Technologies* 89 (2017) 2387-2397. https://doi.org/10.1007/s00170-016-9263-3.

[9] J. Torres, M. Cole, A. Owji, Z. DeMastry, A.P. Gordon, An approach for mechanical property optimization of Fused Filament Fabrication with polylactic acid via design of experiments. *Rapid Prototyping Journal*. 22(2) (2016) 387-404. https://doi.org/10.1108/RPJ-07-2014-0083

[10] J.M. Chacon, M.A. Caminero, E. Garcıa-Plaza, P.J. Nunez, Additive manufacturing of PLA structures using Fused Filament Fabrication: effect of process parameters on mechanical properties and their optimal selection. *Materials & Design*. 124 (2017) 143-157. https://doi.org/10.1016/j.matdes.2017.03.065

[11] H. Li, T. Wang, J. Sun, Z. Yu, The effect of process parameters in Fused Filament Fabrication on bonding degree and mechanical properties. *Rapid Prototyping Journal*. 24(1) (2018) 80-92. https://doi.org/10.1108/RPJ-06-2016-0090

[12] J. Torres, J. Cotelo, J. Karl, A.P. Gordon, Mechanical property optimization of FFF PLA in shear with multiple objectives. *JOM*. 67(5) (2015) 1183-1193. https://doi.org/10.1007/s11837-015-1367-y

[13] A. Lanzotti, M. Grasso, G. Staiano, M. Martorelli, The impact of process parameters on mechanical properties of parts fabricated in PLA with an open-source 3-D printer. *Rapid Prototyping Journal*. 21 (2015) 604-617. https://doi.org/10.1108/RPJ-09-2014-0135

[14] B.M. Tymrak, M. Kreiger, L.M. Pearce, Mechanical properties of components fabricated with open-source 3-D printers under realistic environmental conditions. *Materials & Design*. 58 (2014) 242-246. https://doi.org/10.1016/j.matdes.2014.02.038

[15] E. Ebel, T. Sinnemann, Fabrication of FFF 3D objects with ABS and PLA and determination of their mechanical properties. *RTejournal* 11 (2014). https://www.rtejournal.de/ausgabe11/3872 (accessed 01 June 2020)

[16] S. Brischetto, C.G. Ferro, R. Torre, P. Maggiore, Tensile and Compression Characterization of 3D printed ABS Specimens for UAV Applications. *Proceedings of the 3rd International Conference on Mechanical Properties of Materials (ICMPM)*. IInternational Conference on Mechanical Properties of Materials, Venice, Italy. (2016).

[17] Brischetto, S.; Ferro, C. G.; Maggiore, P.; Torre, R. Compression tests of ABS specimens for UAV components produced via the FFF technique. *Technologies*, **2017**, *5-20*, 1–25.

[18] S. Brischetto, R. Torre, C.G. Ferro, Experimental Evaluation of Mechanical Properties and Machine Process in Fused Filament Fabrication Printed Polymeric Elements. *Advances in Additive Manufacturing, Modeling Systems and 3D Prototyping. AHFE*. 975 (2019) 377-389. https://doi.org/10.1007/978-3-030-20216-3_35

[19] S. Szczepanik, P. Bednarczyk, Bending and compression properties of ABS and PET structural materials printed using FFF technology. *Journal of Casting & Materials Engineering*. 1(2) (2017) 39-42. https://doi.org/10.7494/jcme.2017.1.2.39

[20] T. F. Abbas, F.M. Othman, H.B. Ali, Effect of infill parameter on compression properties in FFF process. *International Journal of Engineering Research and Application*. 7(10) (2017) 16-19. https://doi.org/10.9790/9622-0710021619

[21] L.M. Galatucci, F. Lavecchia, G. Percoco, Study of compression properties of topologically optimized FFF made structured parts. *CIRP Annals - Manufacturing Technology*. 57(1) (2008) 243-246. https://doi.org/10.1016/j.cirp.2008.03.009

[22] S. Kotsmid, P. Beno, Experimental Determination of the Beam Buckling Load. *In Proceedings of TEAM 2018: 9th international scientific and expert conference*. 9th international scientific and expert conference, Novi Sad, Serbia. (2018). ISBN 978-86-6022-098-3

[23] M. Shariati, M. Sedighi, J.; Saemi, H.R. Allahbakhsh, A Numerical and Experimental Study on Buckling of Cylindrical Panels Subjected to Compressive Axial Load. *Journal of Mechanical Engineering*. 66(10) (2010) 609-618.

[24] M. Dundu, Buckling of short cold-formed lipped channels in compression. *Journal of the South African Institution of Civil Engineering*. 56(2) (2014) 46-53. https://scielo.org.za/pdf/jsaice/v56n2/06.pdf (accessed 01 June 2020)

[25] M. He, L. Zheng, Y. Sun, R. Ma, Experimental investigations on mechanical properties and column buckling behavior of structural bamboo. *The Structural Design of Tall and Special Buildings*. 24(7) (2015) 491-503. https://doi.org/10.1002/tal.1176

[26] J. Ye, I. Hajirasouliha, I. Becque, Experimental investigation of local-flexural interactive buckling of cold-formed steel channel columns. *Thin-Walled Structures*. 125 (2018) 245-258. https://doi.org/10.1016/j.tws.2018.01.020

[27] A. Ziolkowski, S. Imielowski, Buckling and post-buckling behaviour of prismatic aluminium columns submitted to a series of compressive loads. *Experimental Mechanics*. 51 (2011) 1335-1345. https://doi.org/10.1007/s11340-010-9455-y

[28] F. Nishino, Y. Ueda, L. Tall, Experimental investigation of buckling of plates with residual stress. *Fritz Laboratory Report*. 290(3) (1966). http://preserve.lehigh.edu/engr-civil-environmental-fritz-lab-reports/173

[29] R. M. Jones, Buckling of Bars, Plates and Shells. *Bull Ridge Publishing*, Virginia, USA, 2006. ISBN: 9780560328219

[30] D. Turkmen, Experimental Investigation of the phenomenon of buckling for steel and aluminium struts. *Journal of Engineering Sciences*. 1(1) (1995) 39-43. ISSN: 1300-7009

[31] C. Bedon, C. Amadio, Flexural–torsional buckling: Experimental analysis of laminated glass Elements. *Engineering Structures*. 73 (2014) 85-99. https://doi.org/10.1016/j.engstruct.2014.05.003

[32] D.T. Borowicz, L.C. Bank, Web buckling in pultruded fiber-reinforced polymer deep beams subjected to concentrated loads. *Journal of Composites for Construction*. 18(3) (2014). https://doi.org/10.1061/(ASCE)CC.1943-5614.0000360

[33] Standard Test Method for Compressive Properties of Rigid Plastics. *Annual Book of ASTM Standards, ASTM International*, West Conshohocken, PA, USA, 2015.

[34] Standard Test Method for Tensile Properties of Plastics. *Annual Book of ASTM Standards, ASTM International*, West Conshohocken, PA, USA, 2014.

[35] Standard Test Method for Tensile Properties of Polymer Matrix Composite Materials. *Annual Book of ASTM Standards, ASTM International*, West Conshohocken, PA, USA, 2017.